

Thermodynamic stability of hard sphere crystals in dimensions 3 through 9

Patrick Charbonneau,^{1,2} Caitlin M. Gish,³ Robert S. Hoy,³ and Peter K. Morse¹

¹*Department of Chemistry, Duke University, Durham, North Carolina 27708*

²*Department of Physics, Duke University, Durham, North Carolina 27708*

³*Department of Physics, University of South Florida, Tampa, Florida 33620*

(Dated: May 3, 2021)

Although much is known about the metastable liquid branch of hard spheres—from low dimension d up to $d \rightarrow \infty$ —its crystal counterpart remains largely unexplored for $d > 3$. In particular, it is unclear whether the crystal phase is thermodynamically stable in high dimensions and thus whether a mean-field theory of crystals can ever be exact. In order to determine the stability range of hard sphere crystals, their equation of state is here estimated from numerical simulations, and fluid-crystal coexistence conditions are determined using a generalized Frenkel-Ladd scheme to compute absolute crystal free energies. The results show that the crystal phase is stable at least up to $d = 9$, and the dimensional trends suggest that crystal stability likely persists well beyond that point.

I. INTRODUCTION

Although the phase behavior of three-dimensional hard spheres was initially debated, for now more than half a century it has been under solid numerical control [1]. As density increases, the liquid branch reaches the liquid-crystal coexistence point, and then splits into a thermodynamically stable crystal branch and a metastable fluid branch. Further densifying the latter gives rise to glasses and eventually to jammed solids [2]. As dimension d increases, these processes are now fairly well understood [3, 4], thanks to the liquid structure then steadily simplifying [5–8]. In low dimensions, however, not only does the local structure markedly impact the metastable liquid properties, it even facilitates crystal nucleation [9, 10]. Because increasing d variously promotes glass formation at the expense of crystallization [10–12], relatively little is known about what happens to the stable crystal branch for $d > 3$. Whether this branch persists in the limit $d \rightarrow \infty$, and whether one can obtain any insight into this limit by considering finite- d systems, remain unclear. The present work aims to shed at least some light on these physical questions.

The primary difficulty of pursuing such a program is that each dimension is endowed with its own particular densest packed (and thus thermodynamically preferred) crystal structure. Previous computational studies [10, 11] have shown that the liquid-crystal coexistence pressure of hard spheres increases with dimension, thus suggesting that the crystal becomes steadily less favorable than the liquid as d increases. This analysis, however, was pursued only over a fairly small dimensional range, and further did not take into account the natural dimensional scaling of the properties of dense liquids. It was furthermore done without proper finite-size scaling considerations, a concerning issue in higher d , wherein computational constraints on system sizes are particularly acute. Questions thus remain as per the robustness of this proposal. Moreover, low-dimensional crystals of hard spheres all have relatively similar physical properties, whereas higher d crystals can exhibit exotic features, such as non-trivial

zero modes [13].

Determining equilibrium conditions for phase coexistence generally implies equating temperature T , pressure P , and chemical potential μ in all phases in presence. Temperature being an irrelevant state variable for hard spheres, situating liquid-crystal (ℓ - s) coexistence then reduces to finding $P_\ell = P_s = P^{\text{coex}}$ and $\mu_\ell = \mu_s = \mu^{\text{coex}}$. Through numerical simulations this determination can be straightforwardly achieved by thermodynamically integrating the equation of state, given a reference free energy for each phase. For hard spheres, the virial expansion provides the liquid equation of state with high precision over a broad d range [14–16], and the ideal gas offers a convenient reference state. The core computational difficulty is for the crystal phase. Its equation of state has been only phenomenologically described (via numerical simulations in low d), and the reference crystal free energy must be obtained from specialized simulation schemes such as that proposed by Frenkel and Ladd [17–19].

In this work, we report the crystal equation of state and the fluid-crystal coexistence conditions for the densest lattice packings in $d = 3$ –9, which are D_3 (face-centered cubic), D_4 , D_5 , E_6 , E_7 , E_8 , and Λ_9 respectively [13]. Added care is given to the consideration of Λ_9 , which is a laminated lattice composed of two interpenetrating D_9 sub-lattices with nontrivial zero modes associated with internal translational degrees of freedom. (This case is particularly informative about higher-dimensional systems, because such modes are present in many other Λ lattices, which are the densest known sphere packing for $9 \leq d \leq 29$, including the highly compact Leech lattice in $d = 24$.) Over the accessible dimensional range, we find that the freezing density φ_f remains well below the (avoided) dynamical transition at φ_d and that the melting density φ_m roughly tracks but also remains below φ_d . We additionally obtain an upper bound on the low-density crystal stability, φ_s^{min} , in each dimension, and find that $\varphi_s^{\text{min}} > \varphi_f$.

The plan for the rest of this article is as follows. Section II defines each of the lattices considered and their embedding in simulations boxes under periodic boundary

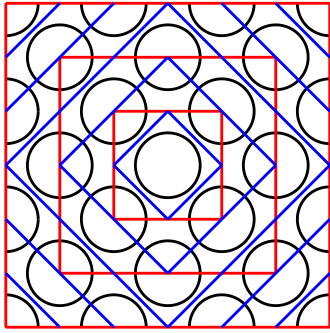


Figure 1. Schematic depiction of commensurability between the simulation box, the crystal symmetry and for disks on a D_2 lattice. Allowed periodic boxes for Z_2 (red) boundary conditions and D_2 (blue) boundary conditions differ. Periodic boxes are shown for $n = 1, 2$, and 3 in Z_2 boundary conditions and $n = 1, 2, 3, 4$, and 5 for D_2 boundary conditions. Clearly, Z_d boundary conditions generically allow fewer system sizes than D_d boundary conditions. Note that while this illustration provides the correct intuition for commensurability in higher dimensions, $d = 2$ is a special case because D_2 boundary conditions are merely a rotated version of Z_2 . No such degeneracy exists in higher d .

conditions. Section III describes how the liquid and crystal equations of state are obtained. Section IV details the calculation of reference state free energies, which leads to phase coexistence results being obtained and described in Sec. V. Section VI briefly summarizes the results and describes possible future research directions.

II. GENERATING AND EMBEDDING HIGH- d CRYSTALS

Densest sphere packings in $d = 3 - 9$ are either related to D -family (checkerboard) lattices or to the E_8 lattice [13]. More specifically, we have:

- the d -dimensional D_d (or checkerboard) lattices contain all points $\{x_1, x_2, \dots, x_d\}$ such that $x_i \in \mathbb{Z}$ and $\sum x_i$ is an even number;
- the E_8 lattice contains two D_8 lattices offset by the eight-dimensional vector $(\frac{1}{2}, \dots, \frac{1}{2})$, such that $E_8 = D_8 \cup (D_8 + (\frac{1}{2})^8)$;
- the E_7 lattice is a seven-dimensional subset of E_8 consisting of points $\{x_1, x_2, \dots, x_8\} \in E_8$ with $\sum x_i = 0$;
- the E_6 lattice is a six-dimensional subset of E_8 consisting of points $\{x_1, x_2, \dots, x_8\} \in E_8$ with $\sum x_i = 0$ and $x_1 + x_8 = 0$. Note that the choice of indices 1 and 8 is arbitrary, but must be kept consistent.
- the D_9^{0+} lattice, which is a specific instance from the continuum of Λ_9 lattices, is analogous to E_8 , in

that it consists of two D_9 lattices offset by a vector $\Xi = \{(\frac{1}{2})^8, \Xi_9\}$, where $\Xi_9 \in \mathbb{R}$.

The points defined by each lattice are used as sphere positions to build the crystal. In the units implied by the lattice distances above, spheres of radius $1/\sqrt{2}$ yield systems at the crystal close packing density, φ_c . Note that, without loss of generality, we here use $\Xi_9 = \frac{1}{2}$ to build the crystal, but the freedom in selecting Ξ_9 translates the existence of an internal zero mode. Additionally, our choice to vary Ξ_9 rather than one of the other components of Ξ is arbitrary, and thus the initial choice of the global degree of freedom is itself nine-fold degenerate. For these reasons D_9^{0+} requires special consideration in numerical simulations as further discussed in Sec. IV C.

Although these crystal definitions may seem straightforward, periodic boundary considerations—which are central to numerical simulations—lead to some geometrical challenges in finding finite-size crystal lattices commensurate with the chosen simulation box. Because only configurations that align with the underlying boundaries are permitted, allowed system sizes, N , are sparse, which presents a numerical hurdle in extrapolating results to the thermodynamic limit, $N \rightarrow \infty$. In this context, embedding crystals inside both standard cubic and various non-cubic boundary conditions conveniently shrinks the size gap between commensurate systems. As discussed in Sec. IV B, finite-size corrections are indeed largely independent of box shape, provided that shape remains (nearly) isotropic.

To see how each crystal can be generated within different boundary conditions, consider first standard Z_d symmetric (cubic) simulations boxes. These boxes naturally accommodate D_3, D_4, D_5, E_8 , and D_9^{0+} , which are derived from integer lattices that have themselves Z_d symmetry. Embedding E_8 and D_9^{0+} in a Z_d box also relies on embedding a D_d lattice, because these lattices simply fill deep holes in D_8 and D_9 , respectively [13]. In practice, the box is chosen to lie on a d -dimensional hypercubic grid with coordinates $[-n, n]$ for $n \in \mathbb{N}$ —thus preventing spurious double counting of a sphere and its periodic image—and each grid point is populated with a sphere if it obeys the even sum rule described above. The resulting commensurability condition is illustrated in Fig. 1, which corresponds to D_d lattices of sizes $N = \frac{1}{2}(2n)^d$. For E_8 and D_9^{0+} , a second lattice is obtained by duplicating and shifting every particle, thus doubling the particle count to $N = (2n)^d$.

Starting from the cubic embedding of any of the above lattices, it is possible to devise an embedding into D_d boundary conditions, and, as a special case, to embed E_8 into E_8 boundary conditions. This construction is here achieved by choosing the D_d (or E_8) boundaries to also have limits $[-n, n]$ that correspond with the blue periodic boxes in Fig. 1. Conway’s decoding algorithms [20, 21] can then be used to find the spheres that lie outside of the boundary and to map their periodic images back into the box. (Duplicate particles are then straightforwardly removed.) This construction results in D_d lattices in D_d

boundary conditions with $N = n^d$, and E_8 lattices in E_8 with $N = n^8$. As with the Z_d boundary conditions, E_8 and D_9^{0+} can be embedded in D_d boundary conditions by simply embedding D_8 or D_9 , respectively, and then inserting a shifted copy of the lattice. This process creates E_8 and D_9^{0+} lattices with $N = 2n^d$. Note that although, in principle, any n is allowed for these constructions, adequately simulating systems larger than a few tens of thousands or particles falls beyond the reach of commonly available computational resources.

Embedding E_6 and E_7 in periodic boxes is slightly less straightforward, but is achieved via generating matrices. An embedding of E_7 crystals in a Z_7 cell follows from the generating matrix (transpose) given by Ref. 13, using all points

$$\mathbf{r} = \begin{bmatrix} 1 & 0 & 0 & 0 & \frac{1}{2} & 0 & 0 \\ 0 & 1 & 0 & 0 & \frac{1}{2} & \frac{1}{2} & 0 \\ 0 & 0 & 1 & 0 & \frac{1}{2} & \frac{1}{2} & \frac{1}{2} \\ 0 & 0 & 0 & 1 & 0 & \frac{1}{2} & \frac{1}{2} \\ 0 & 0 & 0 & 0 & \frac{1}{2} & 0 & \frac{1}{2} \\ 0 & 0 & 0 & 0 & 0 & \frac{1}{2} & 0 \\ 0 & 0 & 0 & 0 & 0 & 0 & \frac{1}{2} \end{bmatrix} \cdot \begin{bmatrix} x_1 \\ x_2 \\ x_3 \\ x_4 \\ x_5 \\ x_6 \\ x_7 \end{bmatrix}. \quad (1)$$

with $x_i \in \mathbb{Z}$ lying inside the \mathbb{Z}_7 cube with integer side lengths $n \geq 2$. This embedding thus produces systems with $N = 8n^7$.

Although E_6 cannot be embedded in Z_6 boundary conditions, it can be embedded in nearly-cubic orthorhombic cells using the *simple-root* generating matrix (transpose) [13]. A first such embedding consists of all points

$$\mathbf{r} = \begin{bmatrix} 1 & 0 & 0 & 0 & 0 & -\frac{1}{2} \\ -1 & 1 & 0 & 0 & 0 & -\frac{1}{2} \\ 0 & -1 & 1 & 0 & 0 & -\frac{1}{2} \\ 0 & 0 & -1 & 1 & 1 & -\frac{1}{2} \\ 0 & 0 & 0 & -1 & 1 & -\frac{1}{2} \\ 0 & 0 & 0 & 0 & 0 & \frac{\sqrt{3}}{2} \end{bmatrix} \cdot \begin{bmatrix} x_1 \\ x_2 \\ x_3 \\ x_4 \\ x_5 \\ x_6 \end{bmatrix}. \quad (2)$$

with $x_i \in \mathbb{Z}$ lying inside of an orthorhombic cell with side lengths $\{1, 1, 1, 1, 1, \frac{\sqrt{3}}{2}\}n$, where $n \geq 4$ and must be even. This embedding produces systems with $N = n^6/2$. A second such embedding has side lengths $\{3, 3, 3, \sqrt{3}, \sqrt{3}, \sqrt{3}\}n$ or $\{3, 3, 3, 2\sqrt{3}, 2\sqrt{3}, 2\sqrt{3}\}$ each containing 24 atoms [10]. Both types are used in this work.

III. LIQUID AND CRYSTAL EQUATIONS OF STATE

This section describes the computational and analytical approaches used to determining the fluid and crystal equations of state.

A. Monte Carlo Simulations

Equilibrium configurations are sampled using a standard Metropolis Monte Carlo (MC) scheme, which defines the unit of time t as one MC cycle. For liquids, we define the structural relaxation time, τ_α , by the characteristic decay of the standard overlap parameter for the chosen MC dynamics [18], and for crystals, we define τ_α by the characteristic time needed for the mean square displacement to reach its plateau [22]. In both cases, systems are deemed equilibrated for simulations run for $t > 10\tau_\alpha$, and 10,000 independent configurations are generated for each density. For the D_9^{0+} crystal the overall equilibration parameters remain the same but additional MC sampling moves are used to accelerate the sampling of its zero modes. More specifically, the Ξ_d degrees of freedom are sampled by using MC moves which displace one D_9 sub-lattice with respect to the other. At the point of maximum degeneracy, $\Xi = \{(\frac{1}{2})^9\}$, nine such pairs of lattices can be created, one for each Ξ_d chosen as the global degree of freedom. Thus, for N single particle moves and 1 center of mass displacements (as motivated in Sec. IV C), 9 relative D_9 subset moves are used, on average, for each MC cycle. In order to preserve the symmetry of the governing Markov chain, each MC move is given equal weight, and thus we sample each MC move with frequency $1/(N + 10)$. These moves are essential for efficiently sampling the D_9^{0+} crystal, as they yield a speedup of at least 10^4 over standard MC (as estimated from the pressure equilibration, or rather the lack thereof).

B. Analytical Forms

Pressure P is extracted from the radial distribution function, $g(r)$. The virial theorem gives the reduced pressure

$$p(\rho) = \frac{\beta P}{\rho} = 1 + 2^{d-1} \varphi g(\sigma^+) \quad (3)$$

at packing fraction $\varphi = \rho\sigma^d V_d$, where V is the box volume, V_d is the d -dimensional volume of a sphere of unit diameter, β is the inverse temperature, and $\rho = \frac{N}{V}\sigma^d$ is the number density of spheres of diameter σ . The value of the pair correlation function at contact, $g(\sigma^+)$, is obtained by extrapolating a quadratic fit of nearby $g(r)$ results. Following standard conventions, all distances are reported for a unit particle diameter, i.e., $\sigma = 1$.

For the liquid, the equation of state is well approximated by the [4, 5] Padé approximant of the virial series

$$p = \frac{1 + \sum_{i=1}^4 b_i \rho^i}{\sum_{i=1}^5 \bar{b}_i \rho^i}. \quad (4)$$

with coefficients b_i and \bar{b}_i [15, 16] obtained from the first 10 virial coefficients computed by Clisby and McCoy [14].

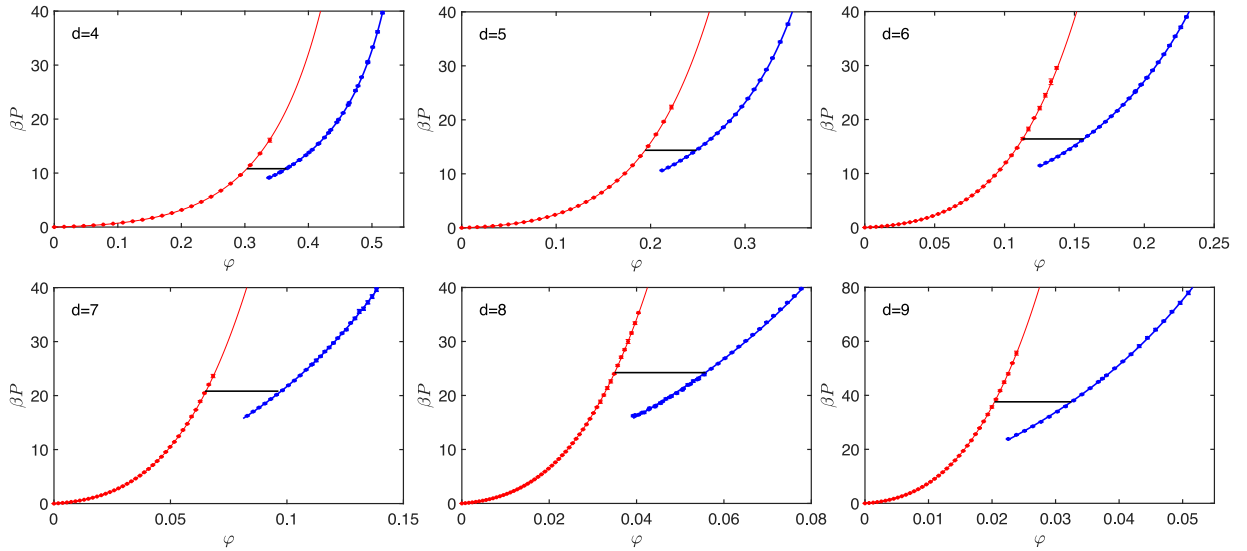


Figure 2. Liquid (red) and crystal (blue) equations of state and coexistence conditions (black) in $d = 4\text{--}9$. Pressures from numerical simulations (points) of the liquid are obtained for $N = 2048, 3888, 5184, 3000, 3840$, and 2000 in $d = 4\text{--}9$ respectively, and are in quantitative agreement with the [4,5] Padé approximant (line) of the virial expansion (Eq. (4)) obtained by Clisby and McCoy [14–16]. Pressures from numerical simulations (points) of the crystal are obtained for $2048, 3888, 5184, 17496, 6561$, and 39366 in $d = 4\text{--}9$ respectively. Fits to the empirical form given in Eq. (5) (solid blue line) quantitatively recapitulate the simulation results. Coexistence conditions are such that $\mu_\ell = \mu_s$ and $P_\ell = P_s$, as described in Sec. V. Error bars denote 95% confidence intervals. Pressure is reported in units that implicitly set the particle diameter to unity, i.e., with $\sigma^d = 1$.

As can be seen in Fig. 2, this form falls within the 95% confidence intervals of the numerical results, at least up to the fluid-crystal coexistence regime. In $d = 3$, in order to obtain an even higher accuracy, we follow the high precision work of Pieprzyk et al. on $\approx 10^6$ particles and use a simple polynomial form that is accurate up to $\varphi = 0.534$.

For the crystal, various equations of state have been proposed [23–25] with careful numerical studies lending greatest credence to that of Speedy in $d = 3$ [24]. Here, the Speedy form with the high-accuracy coefficients of Pieperzyk et al. is used for $d = 3$ [26]. This form, however, is ill-conditioned in higher dimensions. For our purpose, given that the reference point (see Sec. IV B) is by construction close to the melting density, a simple second-order polynomial correction to the free volume scaling suffices,

$$p_s = \frac{1}{1 - \left(\frac{\varphi}{\varphi_c}\right)^{1/d}} + a_0 + a_1 \left(\frac{\varphi}{\varphi_c}\right) + a_2 \left(\frac{\varphi}{\varphi_c}\right)^2, \quad (5)$$

where coefficients a_0 , a_1 , and a_2 are determined by fitting the numerical pressure results. For a given density, the pressure of the liquid is higher than that of the crystal. When a crystal's density is lowered below its lowest stable density, the pressure then rises if a liquid stable is able to nucleate. The lowest stable density φ_s^{\min} is estimated as the lowest density whose pressure does not rise over time. Given the necessity of a liquid nucleation site, the φ_s^{\min} reported here is a lower bound to the true value.

IV. FREE ENERGY DETERMINATION

Given the equation of state, free energy differences can be obtained by thermodynamic integration. In order to obtain absolute values, however, a reference point of known free energy must be available. The efficient selection of such a point depends on the nature of the phase considered. This section describes the various schemes used in this work.

A. Fluid free energy

In the fluid, the (Helmholtz) free energy can be computed using the ideal gas as reference state. The thermodynamic integration can then be written as

$$\frac{\beta F_\ell(\rho)}{N} = \frac{\beta F_{\text{id}}(\rho)}{N} + \int_0^\rho \frac{p-1}{\rho'} d\rho' \quad (6)$$

with the ideal gas free energy given by

$$\frac{\beta F_{\text{id}}}{N} = \ln(\rho \Lambda^d) - 1 + \frac{\ln(2\pi N)}{2N}. \quad (7)$$

Without loss of generality, we set the de Broglie wavelength to unity, $\Lambda = 1$.

B. Crystal free energy

In the crystal phase, a similar thermodynamic integration is possible,

$$\frac{\beta F_s(\rho)}{N} = \frac{\beta F_s(\rho_0)}{N} + \int_{\rho_0}^{\rho} \frac{p}{\rho'} d\rho', \quad (8)$$

albeit using a system of known free energy at number density, ρ_0 . (For numerical efficacy, this density is chosen near an estimate of the melting density.) The free energy of such reference crystal is obtained by Frenkel-Ladd integration from a model crystal which is exactly solvable [17].

Given a reference crystal with energy U_0 and using a coupling parameter $\lambda \in [0, \infty)$, we can write the energy of an alchemical system as

$$U(\lambda) = U_{\text{HS}} + \lambda U_0 \quad (9)$$

where U_{HS} is the hard sphere potential, which is recovered for $\lambda = 0$. The free energy can then be generically written as

$$\frac{\beta F_s(\rho_0)}{N} = -\frac{\beta}{N} \int_0^{\lambda} \langle U \rangle_{\lambda} d\lambda + \frac{\beta F_{\text{corr}}(\rho_0)}{N}, \quad (10)$$

where the subscript λ denotes a thermal average taken at constant λ , and a correction term is added as per Ref. [27]. In the limit $\lambda \rightarrow \infty$, U_0 dominates and the system free energy can be approximated from its contribution alone. In practice, setting a large λ_{max} , allows the integral to be separated as

$$\int_0^{\lambda} \langle U \rangle_{\lambda} d\lambda = F(\lambda > \lambda_{\text{max}}) + \int_0^{\lambda_{\text{max}}} \langle U_0 \rangle_{\lambda} d\lambda, \quad (11)$$

where λ_{max} can be estimated analytically for simple reference systems [18, Eq. 10.3.31]. Note that because $\lambda_{\text{max}} \gg 1$, it is numerically convenient to change integration coordinates as

$$\int_0^{\lambda_{\text{max}}} \langle U_0 \rangle_{\lambda} d\lambda = \lim_{\lambda_{\text{min}} \rightarrow 0^+} \int_{\ln(\lambda_{\text{min}})}^{\ln(\lambda_{\text{max}})} \lambda \langle U_0 \rangle_{\lambda} d(\ln \lambda). \quad (12)$$

The remaining problem is to find a reference crystal whose free energy can be explicitly calculated. The standard solution is to consider an Einstein crystal in which each particle i at position r_i is harmonically tethered to its perfect crystal site, $r_{0,i}$

$$U_0 = \sum_{i=1}^N (\mathbf{r}_i - \mathbf{r}_{0,i})^2. \quad (13)$$

For a non-interacting Einstein crystal the free energy $F_{\text{Ein}} = F(\lambda > \lambda_{\text{max}})$ is given by

$$\frac{\beta F_{\text{Ein}}(\rho_0)}{N} = \frac{d}{2} \ln \left(\frac{\pi}{\lambda_{\text{max}}} \right) + \frac{d}{2N} \ln \left(\frac{N\lambda_{\text{max}}}{\pi} \right), \quad (14)$$

with the correction term [27]

$$\frac{\beta F_{\text{corr}}(\rho_0)}{N} = -\frac{\ln \rho_0}{N} + \frac{d-1}{2} \frac{\ln N}{N}. \quad (15)$$

Note that the center of mass contribution is here treated separately (first term), because it must be kept fixed in numerical simulations. The integrand, $\langle U \rangle_{\lambda} = \langle r^2 \rangle_{\lambda}$, is the mean square displacement of a system equilibrated with an energy given by Eq. (13), which indeed does not permit system-wide translations. In Section IV C, we consider an alternative reference crystal given by a periodic potential whose center of mass is not fixed, and is therefore better suited for the study of Λ_9 .

Numerical integration of the integrand (using a cubic spline smoothing function) chooses λ_{min} such that contributions for $\lambda < \lambda_{\text{min}}$ are negligible, and λ_{max} such that the remainder $\lambda > \lambda_{\text{max}}$ approaches the result for a non-interacting crystal. In practice (see Fig. 3), setting $\lambda_{\text{min}} \approx 10^{-4}$ and $\lambda_{\text{max}} \approx 1400$ suffices. As d increases, the first-order correction used to estimate λ_{max} has a smaller convergence radius, but above λ_{max} the integrand plateaus, hence that portion of the integral can be approximated as $\beta F_{\text{Ein}}/N$, as expected. Note also that the integrand varies smoothly and monotonically, which validates the choice and implementation of the integration scheme.

As Polson et al. have argued [27], the reference free energy scales asymptotically as $1/N$. We thus fit the numerical results to

$$\frac{\beta F(\varphi_0)}{N} = \beta f(\varphi_0) - \frac{\tilde{a}_f}{N} \quad (16)$$

to extrapolate the thermodynamic limit of the reference free energy per particle, $f(\varphi_0)$ (Fig. 4 and Table I). In $d = 3\text{-}6$ and $d = 8$ the number of points used for the fit is ≥ 3 , and thus a statistical error can be reported for βf . For $d = 7$ and 9 only one system is studied, hence a different error estimate must be obtained. Here, we note that the error on βf is the quadrature sum of the error of $\beta F/N$ and \tilde{a}_f/N . Thus, if \tilde{a}_f is bounded from above, a maximum error estimate can be obtained assuming the error and the value of are both equal to the maximum bound. Although the scaling constant \tilde{a}_f exhibits increase with d , it is divided by N in Eq. (16), and the smallest crystal sizes considered in these d are still rather large. The extrapolation error for βf is thus expected to remain small even in $d = 9$. To provide a quantitative estimate, we guess that $\tilde{a}_f \approx 10$ in $d = 7$ and $\tilde{a}_f \approx 100$ in $d = 9$.

With Eq. (16) and the crystal equation of state from Eq. (5), thermodynamic integration in Eq (6) is then used to determine the crystal free energy for conditions near coexistence.

C. Periodic Potential Crystal Reference

As noted in Sec. II, the global internal zero modes along the various Ξ_9 axis of Λ_9 crystals require special

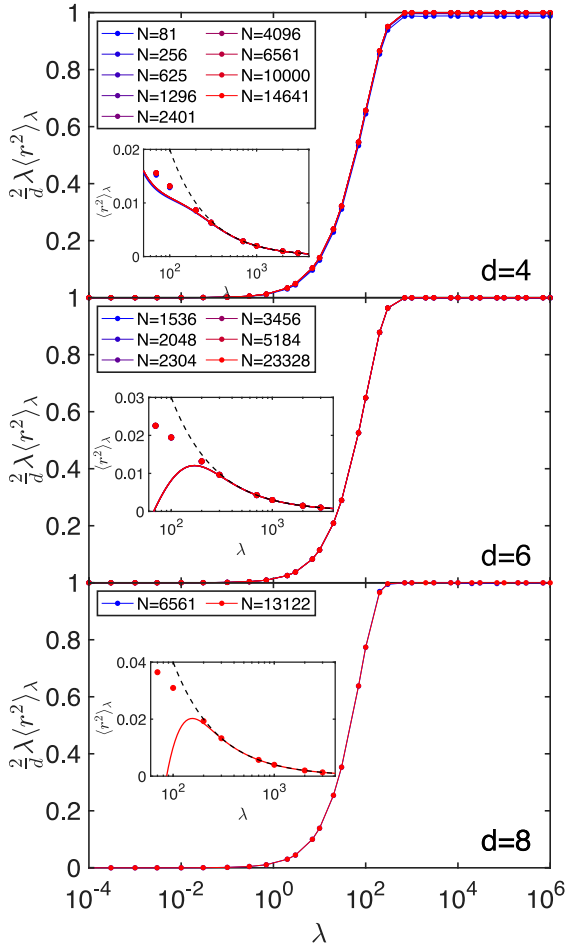


Figure 3. Evolution of the Einstein crystal integrand $\langle U \rangle$ (Eq. (10)) with tethering constant λ in $d = 4, 6$, and 8 . Multiplying the integrand by $2/d$ accounts for the trivial dimensional scaling. Note that finite-size corrections for each integrand scale as $1/N$, and are thus indistinguishable on this scale. For the integration, we choose $\lambda_{\min} = 10^{-4}$, below which the function is essentially 0, and $\lambda_{\max} \approx 1400$ (determined for each crystal using the analytical approach of Ref. [18, Eq. 10.3.31]), such that deviations from an Einstein crystal result in a relative error $1 - \langle r^2 \rangle_\lambda / \langle r^2 \rangle_{\text{Ein},\lambda} \ll 1/N$. These corrections are thus numerically negligible. Insets show the mean square displacement in the Einstein crystal simulations along with the analytic result for the interacting (red line) and non-interacting (black dashed line) Einstein crystal in the large λ limit (black dashed line) [18, Eq. 10.3.30].

consideration. An Einstein crystal reference is inappropriate because particle displacements cannot be bounded in this case. To surmount this issue, we here draw inspiration from the simulation of the crystal phase of parallel cubes. In order to account for the rich collection of zero modes in this model, Groh et al. [28] indeed proposed using a periodic potential crystal that matches the symmetry of the crystal phase of interest as reference.

For example, for all D_d lattices we define the external

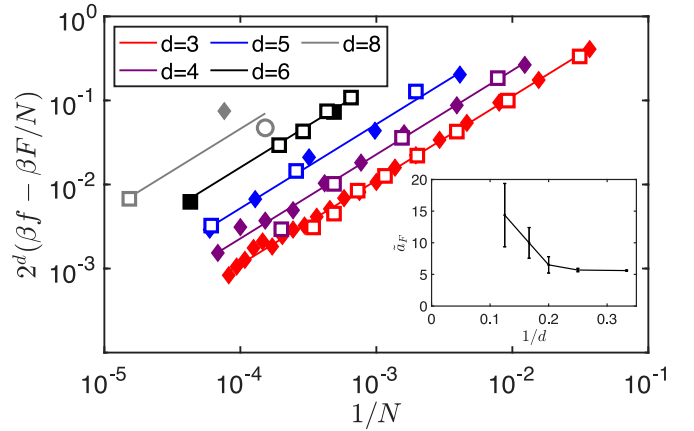


Figure 4. Reference crystal free energy for Z_d (squares), D_d (diamonds) and E_8 (circles) embeddings. For $d = 6$, full and empty squares denote orthorhombic boxes of the first and second types of E_6 embedding, respectively. Because results for a given $d \leq 6$ are essentially colinear, we conclude that (sufficiently isotropic) boundary conditions have little effect on the first-order correction to the intensity of the free energy in this size regime. All results are thus used to fit Eq. (16) (lines), and for the ensuing thermodynamic extrapolation. The sole outlier is E_8 , for which only the smallest box in each embedding type is computationally accessible and is thus more prone to preasymptotic corrections. The larger relative error on the extrapolated thermodynamic free energy reflects this fact. Error bars for 95% confidence intervals are smaller than the symbols and are thus neglected for visual clarity. Curves are offset by a factor of 2^d also for visual clarity. (inset) Dimensional evolution of \tilde{a}_f from Eq. (16).

Table I. Reference crystal excess free energies, $\beta f_{\text{ex}} = \beta f - \beta f_{\text{id}}$, extrapolated in the thermodynamic limit from Eq. (16) with errors denoting 95% confidence intervals in $d = 3\text{--}6$ and 8 , and estimated assuming $\tilde{a}_f \leq 10$ for $d = 7$ and $\tilde{a}_f \leq 100$ for $d = 9$.

d	φ_0	$\beta f_{\text{ex}}(\varphi_0)$
3	0.5450	5.9188(3)
4	0.34	6.2869(4)
5	0.21	7.3840(6)
6	0.14	8.7828(8)
7	0.087	9.806(1)
8	0.048	9.818(15)
9	0.0322	11.83(3)

potential U_0 ,

$$U_0 = \frac{w^2}{8\pi^2} \sum_i^N \left(1 - \prod_{\alpha}^d \cos \left[\frac{2\pi}{w} (\mathbf{r}_i \cdot \hat{x}_{\alpha}) \right] \right) \quad (17)$$

where \mathbf{r}_i is the position of particle i , \hat{x}_{α} is the unit vector in the α direction, and $w = 2\sigma(\varphi_c/\varphi)^{1/d}$ is the lattice spacing.

By contrast to Einstein crystals (Eq. (13)), the crystal center of mass should not be kept fixed but should instead thoroughly sample the system volume. Dedicated center of mass displacements are thus incorporated at

a frequency of $1/N$ relative to individual particle MC moves (Ref. [18, Sec. 3.3]). The finite-size scaling of the free energy is also duly modified,

$$\frac{\beta F_s(\rho_0)}{N} = -\frac{d}{2} \ln \left(\frac{\pi}{\lambda_{\max}} \right) - \frac{\beta}{N} \int_0^{\lambda_{\max}} \langle U_0 \rangle_\lambda d\lambda, \quad (18)$$

where the first term is the free energy of the reference periodic potential crystal, obtained by Taylor expanding around the minimum. By construction, it is equal to the first term in Eq. (14). Note that the second term in that equation, which accounts for the fixed center of mass, is not present because the center of mass is here unconstrained.

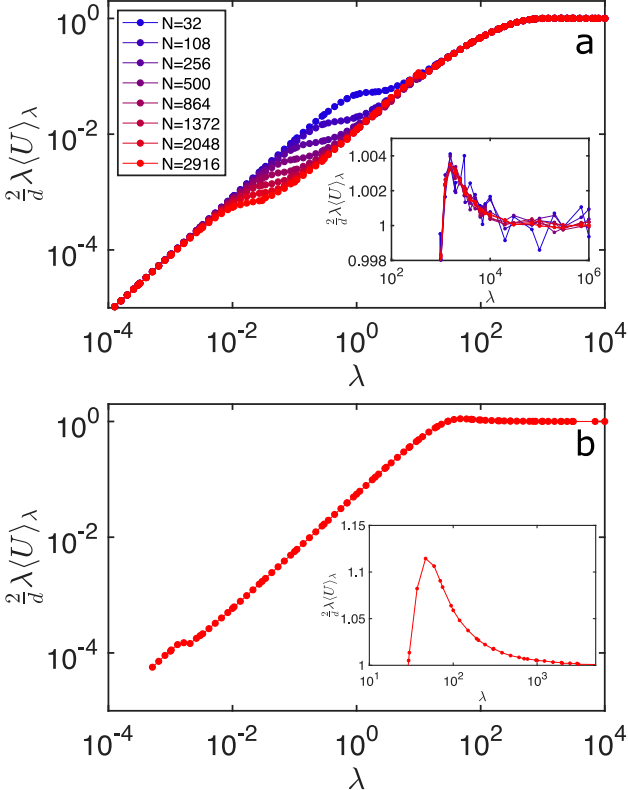


Figure 5. The integrand of Eq. (18) in **a**) $d = 3$ and **b**) $d = 9$ using a periodic reference field on a log-log axis. Umbrella sampling for $\lambda < 1$ ensures that the position of the center of mass samples uniformly the box volume. This enhanced sampling scheme is particularly important near the lower shoulder of the curve, at which point the center of mass gradually untethers from the minima of the external field. (Inset) Close-up on the large λ regime, showing the nonmonotonicity of the integrand, and validating the choice $\lambda_{\max} = 10^6$ for this system.

Validating this approach against the Einstein crystal reference free energies in $d = 3-5$ reveals that a direct application of the periodic potential yields a region of the integrand of Eq. (18) that is particularly challenging to sample. The crossover from unimpeded to limited center of mass displacement is indeed associated with rapidly changing capability to thermally sample energy barriers. An umbrella sampling scheme [18, 29] is thus used

to compensate for this difficulty. Given a non-negative weighting function $\theta(\mathbf{r}^N)$, the ensuing Markov chain distribution

$$\pi(\mathbf{r}) = \frac{\theta(\mathbf{r}) \exp[-\beta U_0(\mathbf{r})]}{\int \theta(\mathbf{r}') \exp[-\beta U_0(\mathbf{r}')] d^d \mathbf{r}'} \quad (19)$$

results in weighted averages of standard thermodynamic quantities. Specifically,

$$\langle U_0 \rangle_\lambda = \frac{\langle U_0 / \theta \rangle_{\lambda, \pi}}{\langle 1 / \theta \rangle_{\lambda, \pi}}, \quad (20)$$

where $\langle \dots \rangle_{\lambda, \theta}$ denotes an average taken at constant λ in the π -weighted ensemble. From Eq. (19), a particularly convenient choice of the weighting function is one that provides an equal probability of being in all states by exactly canceling the Boltzmann weight of the field,

$$\theta(\mathbf{r}) = e^{\beta U_0(\mathbf{r})} \quad (21)$$

This choice results in the position of the center of mass sampling uniformly the whole box volume. Note that although this scheme is appropriate (and efficient) for $\lambda < 1$, the weighting function becomes nearly singular for $\lambda \gg 1$ (see Appendix A). Note also that the crossover from $\lambda \lesssim 1$ to $\lambda \gg 1$ creates a slight overshoot of the integrand of Eq. (18) (Fig. 5 inset). In practice, robust numerical results are obtained by combining the standard periodic potential for $\lambda \geq 1$ with the umbrella sampling scheme for $\lambda < 1$.

For the D_9^{0+} lattice, an additional term is introduced in Eq. (17) to account for the second sub-lattice,

$$U_0 = \frac{w^2}{8\pi^2} \sum_i^N \left(1 - \prod_{\alpha}^d \cos \left[\frac{2\pi}{w} (\mathbf{r}_i \cdot \hat{x}_{\alpha}) \right] \cdot \cos \left[\frac{2\pi}{w} ([\mathbf{r}_i - \Xi] \cdot \hat{x}_{\alpha}) \right] \right), \quad (22)$$

where $\Xi = \{\Xi_d\} = \{(\frac{1}{2})^9\}$ is the chosen offset.

V. COEXISTENCE CONDITIONS

Given the thermodynamic reference free energy along with integrals of the equations of state in Eqs. (4) and (5), the chemical potential can be obtained as

$$\beta\mu(\rho) = \beta f(\rho) + p(\rho). \quad (23)$$

Coexistence conditions $(P^{\text{coex}}, \mu^{\text{coex}})$ can then be determined from the crossing point of parametric plots of μ_L vs P_L and μ_s vs P_s . Freezing and melting densities can then be extracted from the liquid and solid equations of state, respectively.

The coexistence results in Table II lie within the range of previously reported values obtained using a variety of different techniques (Table III) for $d < 6$. However, they differ significantly from previous results reported by one

Table II. Liquid-crystal coexistence parameters for various d reported with 95% confidence intervals, along with reference values for φ_d ($d = 3-8$ [7] and $d = 9$ [21]) and φ_c [13]. Errors for φ_s^{\min} are set by point resolution on the lowest stable configuration.

d	P^{coex}	μ^{coex}	φ_f	φ_m	φ_s^{\min}	φ_d	φ_c
3	11.578(3)	16.082(4)	0.4919(3)	0.5434(4)	0.5142(16)	0.5770(5)	0.7405
4	10.807(3)	15.133(3)	0.3031(3)	0.3653(3)	0.324(16)	0.4036(2)	0.6169
5	14.363(3)	17.604(3)	0.1942(1)	0.2484(3)	0.206(6)	0.2683(1)	0.4653
6	16.400(4)	17.697(3)	0.1129(1)	0.1567(2)	0.125(5)	0.1723(1)	0.3729
7	20.43(1)	18.26(1)	0.0648(1)	0.0963(2)	0.080(2)	0.1076(1)	0.2953
8	24.23(9)	17.82(4)	0.0350(5)	0.0558(2)	0.0392(11)	0.06585(5)	0.2537
9	37.6(1)	20.0(1)	0.020(2)	0.032(3)	0.0225(12)	0.0391(6)	0.1458

of us [10], which did not consider finite-size corrections and were numerically somewhat crude. In $d \geq 6$, however, our results markedly differ from those of all previous reports. A possible reason for this departure is that these earlier estimates did not directly probe the thermodynamics of coexistence, but opted either for estimates that have limited first-principle support: a mean-field description of caging, Mean-Field Caging Theory (MFCT) [30], and matching features of $g(r)$ between coexisting phases [31].

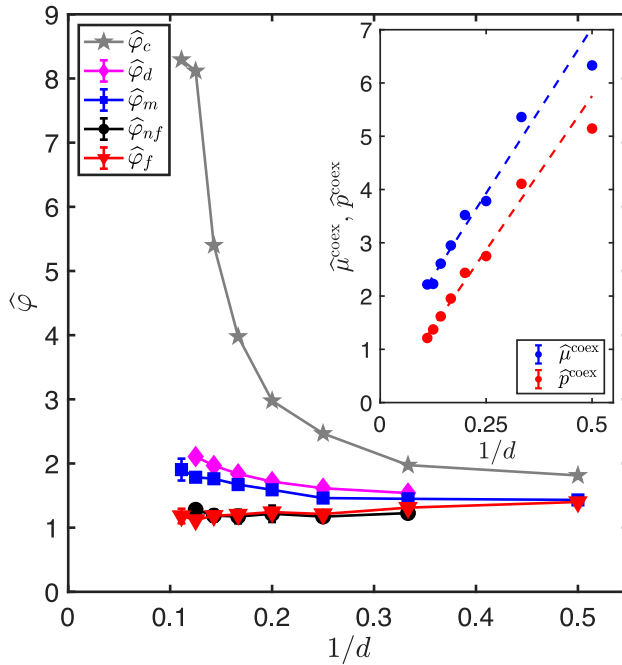


Figure 6. Asymptotically scaled freezing $\widehat{\varphi}_f$ and melting $\widehat{\varphi}_m$. While $\widehat{\varphi}_f$ appears to tend to a constant equal to the onset of non-Fickian diffusion $\widehat{\varphi}_{nf}$, $\widehat{\varphi}_m$ steadily increases with d , seemingly tracking the (avoided) dynamical glass transition φ_d (from Refs. 21 and 32). Data for $d = 2$ are obtained by combining the liquid-hexatic coexistence density reported in Ref. 33 with the liquid equation of state given by the [4, 5] Padé approximant of the virial expansion in Ref. 14. (Inset) Dimensional evolution of the similarly scaled coexistence pressure $\widehat{p} = \beta P/(\rho_e d)$ and chemical potential $\widehat{\mu}$. Dashed lines are guides to the eye.

In order to compare densities and pressures across di-

mensions, we consider and correct for their asymptotic $d \rightarrow \infty$ scaling, using results for the dense liquid state [3]. We thus consider rescaled reduced pressures $\widehat{p} = p/d$, rescaled chemical potentials $\widehat{\mu} = \beta\mu/d$, and rescaled densities $\widehat{\varphi} = 2^d \varphi/d$. In this form, the melting and freezing densities suggest an interesting physical picture (Fig. 6a). Even though the lattice close packing density grows rapidly with d , the freezing point fluctuates around a constant, $\widehat{\varphi}_f \approx 1.3$. Interestingly, this observation is consistent with the recent phenomenological observation that φ_f and the onset of non-Fickian diffusion φ_{nf} (nearly) coincide in $d = 3$ [34]. It also stands in stark contrast with the predictions of MFCT [30],

$$\widehat{\varphi}_f^{\text{MFCT}} = \frac{\widehat{\varphi}_c(1+2d)}{2 + \widehat{\varphi}_c \frac{2d^2}{V_d}} \xrightarrow{d \rightarrow \infty} \frac{V_d}{d} \rightarrow 0. \quad (24)$$

While the freezing point thus lies well below the (avoided) dynamical transition φ_d , the melting point φ_m approaches, yet remains below, φ_d in all d considered. Taken together with the coexistence pressure and chemical potential results, these observations suggest that hard sphere crystallization—albeit rare—is not significantly impeded by the slowdown of the fluid dynamics for $d \leq 9$. Using the crude estimate $\widehat{\varphi}_f \approx 1.3$, and the high dimensional equation of state $\widehat{p} = \frac{\widehat{\varphi}}{2}$ we can also extrapolate the $d \rightarrow \infty$ fluid-crystal coexistence conditions as $\widehat{\mu}^{\text{coex}} \approx 0.65$. Applying thermodynamic integration in this limit then yields $\widehat{\mu} = 2\widehat{p}$, and thus $\widehat{\mu}^{\text{coex}} \approx 1.3$. This prediction, however, deviates from the extrapolated lines in Fig. 6, implying that, as d increases, either the scaling of the pressure and chemical potential becomes nonlinear or $\widehat{\varphi}_f$ decreases. Without guidance from a proper theory of mean-field crystallization to account for the evolving crystal symmetry with d , further speculation remains rather tentative.

This scaling form nevertheless suggests a rough description of the relative stability of crystals across the dimensions considered. For $d \leq 9$, odd- d crystals have coexistence pressures and chemical potentials which lie below the trend line, while those of their even- d counterparts lie above it. The latter are therefore relatively more thermodynamically stable than the former, with E_8 crystal being a noted example as its $\widehat{\mu}^{\text{coex}}$ lies well below the overall trend. This feature likely reflects E_8 being in a sense the densest sphere lattice for $d > 1$, given its

near saturation of the Rogers bound [35] and its actual saturation of the more strict Cohn-Elkies bound [36–38].

Another form of crystal (meta)stability is the resistance to melting below the coexistence pressure. In order for a homogeneous crystal to melt, a (rare) nucleation site must typically form. The free energy barrier that controls this activated process is, however, expected to vanish at a spinodal-like point, below which the crystal is truly unstable. Our simulations provide an upper bound for this last quantity, φ_s^{\min} (Table II). We note that although the gap between the freezing density and φ_s^{\min} shrinks with dimension, the two quantities are distinct, and $\varphi_f < \varphi_s^{\min}$ even in $d = 9$. These observations thus suggest that the coexistence estimate used in Ref. 11, which relies on this instability in $d = 4\text{--}6$, would likely fall far off the mark were it applied to the higher d crystals.

VI. CONCLUSION

From this analysis, it is clear that the crystal phase is thermodynamically stable at high pressures in dimensions $d = 3\text{--}9$. It also appears that \hat{p}^{coex} and $\hat{\mu}^{\text{coex}}$ tend smoothly towards finite values in the limit $d \rightarrow \infty$. Given our scheme for the Λ_9 lattice and relatively weak dimensional dependence of \tilde{a}_f , generalizing our study to the non-root lattices that dominate in $d > 8$ [13] should be conceivable. The minimal system sizes needed for these studies, however, are too computationally prohibitive for the moment.

With coexistence conditions firmly established in $d = 3\text{--}9$, questions about the dimensional evolution of nucleation and melting nevertheless persist. Because $\hat{\varphi}_f$ appears to be dimensionally invariant, it remains to be shown what factor actually controls the height of the crystallization barrier in high-dimensional systems. Computing the solid-liquid interfacial free energy [46–48] would further enlighten this trend. This effort, however, is left for future work.

Our methodological improvements for the periodic potential crystal reference should also find applications in a variety of more common two- and three-dimensional systems. For instance, it could be used to revisit the phase behavior of parallel cubes as well as for exploring that of a number of crystals of polyhedra [49] and superballs [50] that exhibit comparable zero modes.

ACKNOWLEDGMENTS

We thank Yi Hu, Irem Altan, and Francesco Zamponi for fruitful discussions. This work was supported by grants from the Simons Foundation (#454937, Patrick Charbonneau) and from the National Science Foundation under Grant DMR-2026271 (Robert Hoy). The computations were carried out on the Duke Compute Cluster (DCC), for which the authors thank Tom Milledge's assistance. Data relevant to this work have been archived

Table III. Previously reported coexistence conditions in order of publication for each dimension. Estrada et al. [31] obtained an estimate using polynomial fitting (PF) and another using universal relations (UR), denoted accordingly. Values reported without error bars are from publications in which they were not provided. Results from this work are given in bold.

d	P^{coex}	μ^{coex}	φ_f	φ_m	Ref.
3	11.70(18)	–	0.494(2)	0.545(2)	[39]
	–	–	0.487	–	[40]
	11.564	17.071	0.494	0.545	[18]
	11.55(11)	–	0.491(1)	0.543(1)	[41]
	11.49(9)	–	0.489(2)	0.540(2)	[42]
	–	–	0.494	–	[30, 43, 44]
	11.54(4)	–	–	–	[45]
	11.202	–	0.488(5)	0.537	[31] PF
	11.668	–	0.492	0.542	[31] UR
	11.5712(10)	16.0758(20)	0.49176(5)	0.54329(5)	[26]
4	11.578(3)	16.082(4)	0.4919(3)	0.5434(4)	
	–	–	0.308	–	[30, 40]
	–	–	0.32(1)	0.39(1)	[11]
	9.15	13.7	0.288	0.337	[10]
	11.008	–	0.304(1)	0.368	[31] PF
	11.469	–	0.308	0.374	[31] UR
5	10.807(3)	15.133(3)	0.3031(3)	0.3653(3)	
	–	–	0.194	–	[40]
	–	–	0.169	–	[30]
	–	–	0.20(1)	0.25(1)	[11]
	10.2	14.6	0.174	0.206	[10]
	13.433	–	0.190(1)	0.242	[31] PF
6	13.184	–	0.189	0.240	[31] UR
	14.363(3)	17.604(3)	0.1942(1)	0.2484(3)	
	–	–	0.084	–	[30]
	13.3	16.0	0.105	0.138	[10]
7	16.668	–	0.114(2)	0.146	[31] PF
	17.0318	–	0.114	0.147	[31] UR
	16.400(4)	17.697(3)	0.1129(1)	0.1567(2)	
	–	–	0.039	–	[30]
8	22.597	–	0.0702(2)	0.086	[31] PF
	22.1569	–	0.0696	0.085	[31] UR
	20.43(1)	18.26(1)	0.0648(1)	0.0963(2)	
9	–	–	0.017	–	[30]
	–	–	0.0427	–	[31] UR
	24.23(9)	17.82(4)	0.0350(5)	0.0558(2)	
9	37.6(1)	20.0(1)	0.020(2)	0.032(3)	

and can be accessed at the Duke Digital Repository [51].

Appendix A: Free energy of a single particle in the periodic reference crystal field

A minimal model of the periodic potential crystal reference calculation is a single particle evolving in the field given by Eq. (17) (see Fig. 5). Because the problem can then be solved analytically, it provides a robust benchmark for the numerical implementation and its optimization.

The integrand of Eq. (18) can then be written explicitly

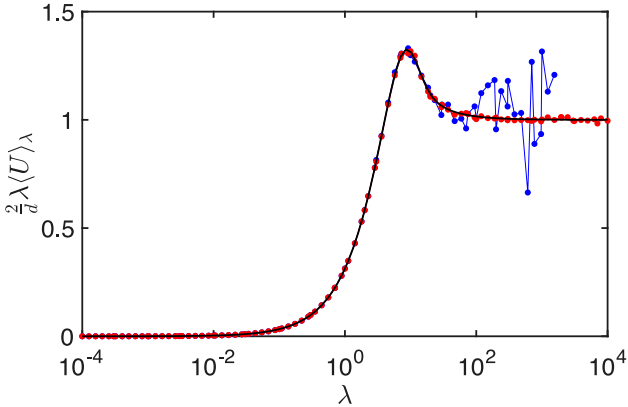


Figure 7. Integrand of Eq. (18) for a single particle in the periodic $d = 3$ reference crystal from direct integration (black line), direct simulation of the periodic potential (red points), and simulation of the umbrella potential of Eq. (20) (blue points). The different results are indistinguishable below $\lambda \approx 10$, but for $\lambda \gtrsim 10$ results from the umbrella potential deviate from the correct solution due to poor sampling of the bottom of the potential well, wherein the particle is then largely confined.

as

$$\langle U(\mathbf{r}, \lambda') \rangle_{\lambda'} = \frac{\int U(\mathbf{r}, \lambda') \exp[-\beta U(\mathbf{r}, \lambda')] d^d \mathbf{r}}{\int \exp[-\beta U(\mathbf{r}, \lambda')] d^d \mathbf{r}}, \quad (\text{A1})$$

and thus the free energy is $\beta F = -\beta \int_0^\lambda \langle U(\mathbf{r}, \lambda') \rangle_{\lambda'} d\lambda$. Although the integrand lacks a closed form expression for $d > 1$, it can be evaluated numerically with very high accuracy for any λ and d . The results for $d = 3$ serve as an analytical reference in Fig. 7. Equivalently, the free energy can be computed directly from the standard statistical mechanics expression, $\beta F = -\ln Z$, for the

partition function Z , and hence

$$\beta F = -\ln \int \exp[-\beta U(\mathbf{r}, \lambda)] d^d \mathbf{r}. \quad (\text{A2})$$

This expression also does not have a closed form, but can be calculated numerically with high accuracy.

These quantities can be used to benchmark the standard Monte Carlo sampling of the periodic potential as well as by the umbrella sampling scheme described in Sec. IV C. For $\lambda \gg 1$ standard Monte Carlo sampling leaves the particle trapped at the bottom of one of the wells, but as λ decreases the particle regularly explores barriers and crosses over into neighboring wells. Given sufficient sampling, the intermediate λ regime is recovered (see Fig. 7), and thus the various features of the direct integration are recapitulated.

This outcome contrasts with Monte Carlo simulations that use the umbrella sampling approach of Eq. (21). In this case, the particle samples all points in the box with equal probability, even though the actual contribution to the partition function of each point is proportional to its Boltzmann weight, $\exp[-\lambda \beta U]$. In the single particle case, both simple Monte Carlo and umbrella sampling work well for $\lambda \lesssim 10$. However, for $N > 1$ and $\lambda \sim 1/N$ standard Monte Carlo sampling fails because it then becomes rare for simulations to produce particles which are near the top of energy barriers, whose contributions remain important for accurately calculating the free energy.

For $\lambda \gg 1$, the Boltzmann weight $\exp[-\lambda \beta U]$ concentrates, and the only significant contributions to Z come from a small collection of (degenerate) points in phase space, i.e., the bottom of each well. Both the numerator and the denominator of Eq. (20) diverge in this limit, which makes the evaluation numerically unstable. Physically, this instability corresponds to $\langle U \rangle$ being vastly undersampled compared with other λ regimes, thus leading to marked deviation from the exact result (Fig. 7).

This analysis motivates the high λ cutoff used in the umbrella sampling for $N > 1$. Because the Boltzmann weight $\exp[-\lambda \beta \sum_i U_i]$ acts on the total energy, the same cutoff of $\lambda = 1$ can be used. However, as N grows, it is important to sum these contributions carefully, because θ then also grows.

[1] G. Battimelli, G. Ciccotti, and P. Greco, *Computer Meets Theoretical Physics: The New Frontier of Molecular Simulation*, The Frontiers Collection (Springer International Publishing, 2020).

[2] P. Charbonneau, J. Kurchan, G. Parisi, P. Urbani, and F. Zamponi, *Annu. Rev. Condens. Matter Phys.* **8**, 265 (2017).

[3] G. Parisi and F. Zamponi, *Rev. Mod. Phys.* **82**, 789 (2010).

[4] G. Parisi, P. Urbani, and F. Zamponi, *Theory of Simple Glasses: Exact Solutions in Infinite Dimensions* (Cambridge University Press, 2020).

[5] B. Charbonneau, P. Charbonneau, and G. Tarjus, *Phys. Rev. Lett.* **108**, 035701 (2012).

[6] B. Charbonneau, P. Charbonneau, and G. Tarjus, *J. Chem. Phys.* **138**, 12A515 (2013).

[7] P. Charbonneau, Y. Jin, G. Parisi, and F. Zamponi, *Proc. Natl. Acad. Sci. U.S.A.* **111**, 15025 (2014).

[8] M. Mangeat and F. Zamponi, *Phys. Rev. E* **93**, 012609 (2016).

[9] J. A. van Meel, D. Frenkel, and P. Charbonneau, *Phys. Rev. E* **79**, 030201 (2009).

[10] J. A. van Meel, B. Charbonneau, A. Fortini, and P. Charbonneau, *Phys. Rev. E* **80**, 061110 (2009).

- [11] M. Skoge, A. Donev, F. H. Stillinger, and S. Torquato, Phys. Rev. E **74**, 041127 (2006).
- [12] P. Charbonneau, A. Ikeda, J. A. van Meel, and K. Miyazaki, Phys. Rev. E **81**, 040501 (2010).
- [13] J. H. Conway and N. J. A. Sloane, *Sphere Packings, Lattices and Groups*, 2nd ed., Grundlehren der mathematischen Wissenschaften (Springer-Verlag, New York, 1993).
- [14] N. Clisby and B. M. McCoy, J. Stat. Phys. **122**, 15 (2006).
- [15] M. Bishop and P. A. Whitlock, J. Chem. Phys. **123**, 014507 (2005).
- [16] L. Lue and M. Bishop, Phys. Rev. E **74**, 021201 (2006).
- [17] D. Frenkel and A. J. C. Ladd, J. Chem. Phys. **81**, 3188 (1984).
- [18] D. Frenkel and B. Smit, *Understanding Molecular Simulation: From Algorithms to Applications*, 2nd ed. (Academic Press, New York, 2001).
- [19] V. Khanna, J. Anwar, D. Frenkel, M. F. Doherty, and B. Peters, J. Chem. Phys. **154**, 164509 (2021).
- [20] J. Conway and N. Sloane, IEEE Trans. Inf. Theory **28**, 227 (1982).
- [21] P. Charbonneau, Y. Hu, J. Kundu, and P. Morse, *In preparation* 2021.
- [22] P. Charbonneau, P. Morse, W. Perkins, and F. Zamponi, *In preparation* 2021.
- [23] K. R. Hall, J. Chem. Phys. **57**, 2252 (1972).
- [24] R. J. Speedy, J. Phys. Condens. Matter **10**, 4387 (1998).
- [25] P. Tarazona, Phys. Rev. Lett. **84**, 694 (2000).
- [26] S. Pieprzyk, M. N. Bannerman, A. C. Braňka, M. Chudak, and D. M. Heyes, Phys. Chem. Chem. Phys. **21**, 6886 (2019).
- [27] J. M. Polson, E. Trizac, S. Pronk, and D. Frenkel, J. Chem. Phys. **112**, 5339 (2000).
- [28] B. Groh and B. Mulder, J. Chem. Phys. **114**, 3653 (2001).
- [29] G. M. Torrie and J. P. Valleau, J. Comput. Phys. **23**, 187 (1977).
- [30] X.-Z. Wang, J. Chem. Phys. **122**, 044515 (2005).
- [31] C. D. Estrada and M. Robles, J. Chem. Phys. **134**, 044115 (2011).
- [32] P. Charbonneau, A. Ikeda, G. Parisi, and F. Zamponi, Phys. Rev. Lett. **107**, 185702 (2011).
- [33] M. Engel, J. A. Anderson, S. C. Glotzer, M. Isobe, E. P. Bernard, and W. Krauth, Phys. Rev. E **87**, 042134 (2013).
- [34] J. Ruiz-Franco, E. Zaccarelli, H. J. Schöpe, and W. van Megen, J. Chem. Phys. **151**, 104501 (2019).
- [35] C. A. Rogers, Proc. London Math. Soc. **s3-8**, 609 (1958).
- [36] H. Cohn and N. Elkies, Ann. Math. **157**, 689 (2003).
- [37] M. S. Viazovska, Ann. Math. **185**, 991 (2017).
- [38] H. Cohn, Not. Am. Math. Soc. **64**, 102 (2017).
- [39] W. G. Hoover and F. H. Ree, J. Chem. Phys. **49**, 3609 (1968).
- [40] J. P. J. Michels and N. J. Trappeniers, Phys. Lett. A **104**, 425 (1984).
- [41] R. J. Speedy, J. Phys.: Condens. Matter **9**, 8591 (1997).
- [42] N. B. Wilding and A. D. Bruce, Phys. Rev. Lett. **85**, 5138 (2000).
- [43] B. J. Alder and T. E. Wainwright, J. Chem. Phys. **27**, 1208 (1957).
- [44] G. Bryant, S. R. Williams, L. Qian, I. K. Snook, E. Perez, and F. Pincet, Phys. Rev. E **66**, 060501 (2002).
- [45] C. Vega and E. G. Noya, J. Chem. Phys. **127**, 154113 (2007).
- [46] D. Richard and T. Speck, J. Chem. Phys. **148**, 224102 (2018).
- [47] D. Richard and T. Speck, J. Chem. Phys. **148**, 124110 (2018).
- [48] M. Bültmann and T. Schilling, Phys. Rev. E **102**, 042123 (2020).
- [49] P. F. Damasceno, M. Engel, and S. C. Glotzer, Science **337**, 453 (2012).
- [50] R. D. Batten, F. H. Stillinger, and S. Torquato, Phys. Rev. E **81**, 061105 (2010).
- [51] “Duke digital repository,” <https://doi.org/10.7924/xxxxxxxxxx>.